Supporting Information

Radical-mediated Conversion of Methane and Water to Light Alcohols

Zeyu Gao,[1] Di Li,[2] Yuping Yang,[1] Chenxin Wu,[3,4] Li Wang,[5] Zhaolun Cui,[6]* Lei Hua,[3,4] Haiyang Li,[3,4] Chong Peng,[1] Dehui Deng,[2,7]* Yanhui Yi[1]*

[1] State Key Laboratory of Fine Chemicals, Frontier Science Center for Smart Materials, School of Chemical Engineering, Dalian University of Technology, Dalian 116024, P.R. China.
[2] State Key Laboratory of Catalysis, Collaborative Innovation Center of Chemistry for Energy Materials, Dalian Institute of Chemical Physics, Chinese Academy of Sciences, Dalian 116023, P.R. China.
[3] State Key Laboratory of Medical Proteomics, Dalian Institute of Chemical Physics, Chinese Academy of Sciences, Dalian 116023, P.R. China.
[4] Liaoning Key Laboratory for Mass Spectrometry Technology and Instrumentation, Dalian 116023, P.R. China.
[5] College of Environmental Sciences and Engineering, Dalian Maritime University, Dalian 116026, P.R. China.
[6] Key Lab of Materials Modification by Laser, Ion, and Electron Beams, Dalian University of Technology, Dalian 116024, P.R. China.
[7] University of Chinese Academy of Sciences, Beijing 100049, P.R.China.
Email: yiyanhui@dlut.edu.cn

Table of Contents

1. Experimental setup

As scheme S1 shows, water vapor (120 ml/min) was supplied by a steam generator (FD-HG from fad laboratory equipment Co. Ltd.) at 115 ℃ vaporization temperature, and the flow rate of water vapor was controlled by an injection pump. CH_4 (30 ml/min) and Ar (60 ml/min) were monitored by mass flow controllers, and the three gases were homogeneously mixed before passing through the plasma reactor. There are two caveats to the experiments.

Firstly, the gas line must be heated with a heating ribbon to avoid condensation of the water vapor. Because liquid state of water not only leads to non-uniformity mixing of CH_4 and H_2O, being conducive to C-C coupling reaction of CH_4 for C_2H_6 production in partial space of the reactor with abundant CH_4 but scarce H_2O. To avoid the above mentioned problems in this study, we used a steam generator to supply water vapor, which was homogeneously mixed with CH_4 and Ar before passing through the plasma reactor. In addition, the gas line was heated with a heating ribbon, and the temperature was maintained at 115 ℃ to avoid condensation of the water vapor.

Secondly, noble gases (Ar) was added into the feed stock to improve the discharge through Penning ionization. Generally, DBD discharge is inhibited by electron affinity of H_2O molecules, which is not favorable for activation of H_2O molecules. Thus DOM was relatively inhibited but C-C coupling reaction of CH_4 for C_2H_6 production was relatively enhanced when noble gas is absent. Therefore, in this paper, Ar was added into the feed stock to improve the DBD, and thus improve activation of H_2O molecules for DOM.

The gaseous products were analyzed by an on-line gas chromatograph (Tianmei GC-7900, TDX-01 column, alumina-filled column) equipped with a thermal conductivity detector (TCD) and a flame ionization detector (FID). The discharge frequency was fixed at 9.3 kHz and the discharge voltage was kept at about 7.5 kV. The discharge voltage and current were measured by a digital fluorescence oscilloscope (Tektronix, DPO 3012) with a high voltage probe (Tektronix P6015) and a current probe (Pearson 6585). Liquid products were collected by a cold trap (a mixture of isopropanol and liquid nitrogen at temperatures below -120 ℃) and then analyzed by GC-2014C (Shimadzu, polyethylene glycol-2000 column) and GC-MS (Agilent 5975C, DB-1701 column). A GC-2014C instrument equipped with a FID was used to measure products species. A Durabond (DB-1) wax column with a polar substrate was used to support aqueous injections. The column was 320 μm thick and 30 m long and installed in an oven. The GC temperature program was set to 40 ℃ at the time of injection followed by a linear ramp of 10 ℃ /min to 150 ℃ (2 min hold time) and a second linear ramp of 10 ℃/min to 220 ℃ (15 mins hold time). Hydrogen was used as the carrier gas with a constant flow rate (1ml/min) and nitrogen was used as the make-up gas. A split/splitless inlet was used (50:1 split ratio) with an inlet pressure of 50 kPa and an inlet temperature of 220 ℃. An inlet liner containing glass wool was used to ensure uniform vaporization of water. Unknown samples were analyzed with gas injection volumes of 100 μl (using a Hamilton gas-tight 1700 series syringe with a cemented 22 gauge needle and point style 5 with a 1700 series chaney adapter to lower the uncertainty in gaseous injection to ~1%) and aqueous injections were 1 μl to keep the column and the inlet from getting damaged.

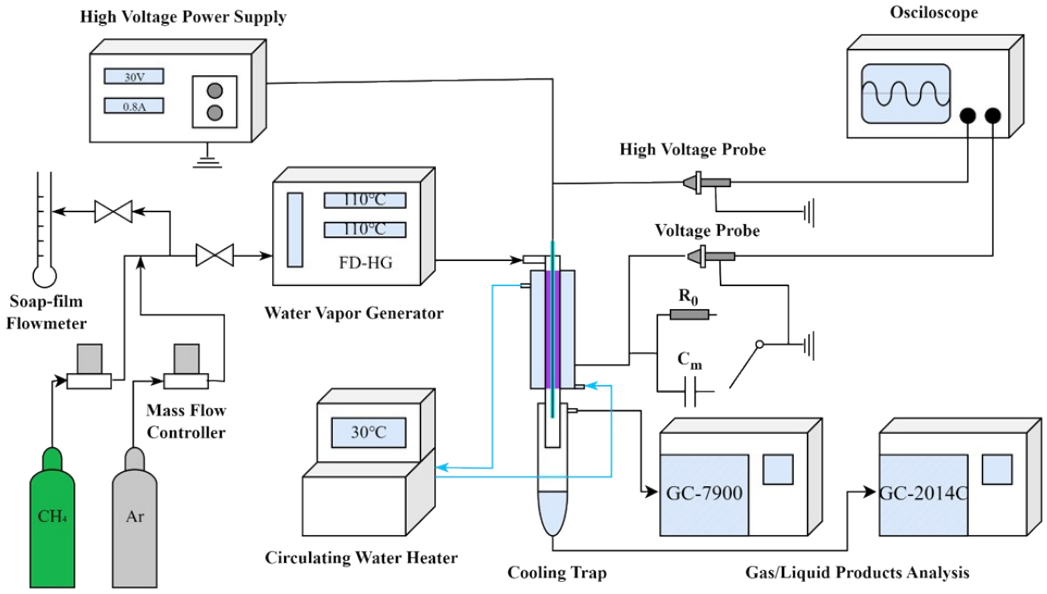

Scheme S1. Experimental setup for the $CH_4/Ar/H_2O$ plasma reaction.

2. The structural of the optimized DDBD reactor

A self-designed coaxial cylindrical DDBD reactor was employed in this study. The configuration incorporated a high-voltage metal electrode (2 mm in outer diameter) and two layers of quartz glass as dielectrics (wall thickness: 1 mm). These components defined a 2-mm discharge gap and an effective discharge length of 5 cm. The reactor was cooled by circulating water maintained at 25 ℃ to ensure a stable temperature within the plasma zone. Reactant gases were fed into the reactor via a top-mounted inlet, and the effluent was passed through a cold trap for product collection.

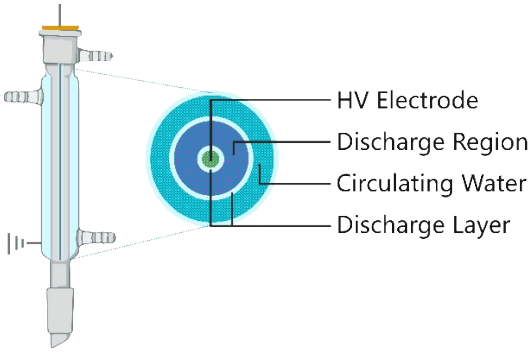

Scheme S2. The structural of the optimized DDBD reactor.

3. Effect of electric field distribution

To evaluate the optimization of the electric field distribution, the discharge characteristics of the single dielectric barrier discharge (SDBD) and double dielectric barrier discharge (DDBD) reactors were systematically compared. Figure S1(A) presents the Lissajous figures for both configurations, illustrating their distinct electrical behaviors and power dissipation. Figure S1(B) displays the corresponding discharge waveforms, capturing the temporal evolution of the discharge pulses. To further elucidate the fundamental differences in their discharge mechanisms, the statistical distributions of the discharge filament intensities were quantitatively analyzed, as shown in Figures S1(C) and S1(D).

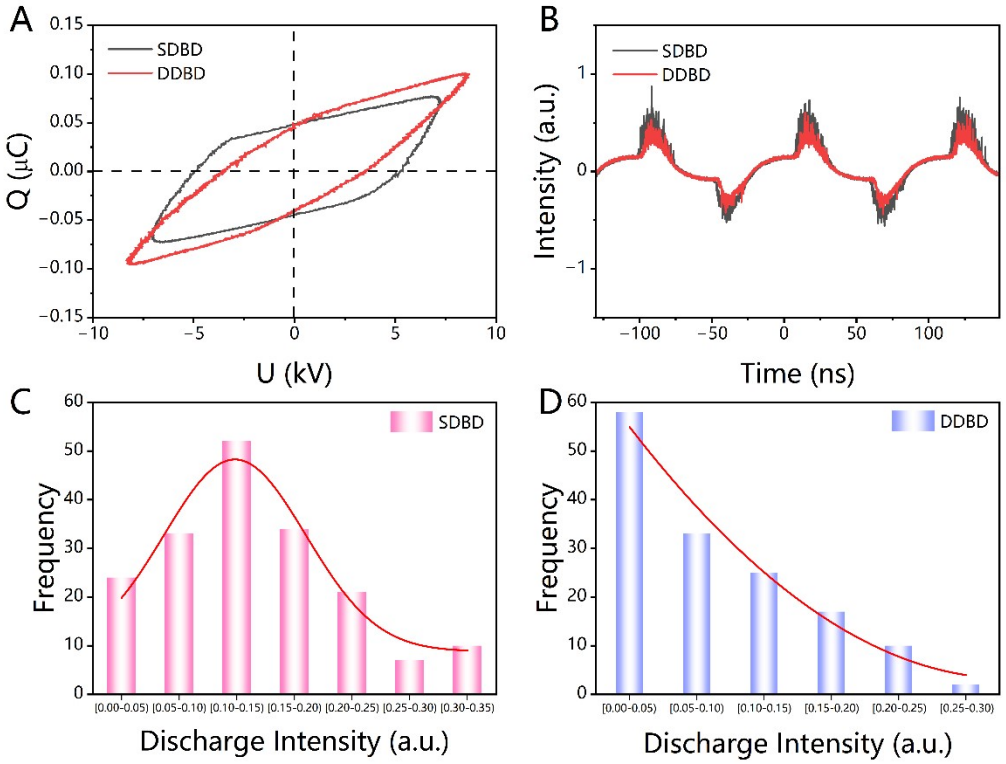

Figure S1. Comparison of discharge characteristics between SDBD and DDBD. (A) Lissajous figures of the SDBD and DDBD reactors; (B) Discharge waveforms of the SDBD and DDBD reactors; Statistical distribution of the discharge filament intensity between the (C) SDBD reactor and (D) DDBD reactor.

4. Effect of thermal management

To evaluate the operational stability of the reactor and elucidate the crucial role of temperature control, a 100-minute continuous operation test was conducted. We systematically compared the performance of the present DDBD equipped with a recirculating cooling water system (RCWS) against a conventional uncooled DDBD under identical initial discharge conditions. During this extended operation, the temperature variation in the reaction zone was monitored in real time. Simultaneously, the evolution trends of CH_4 conversion, liquid products selectivity, and gas products selectivity were recorded. This comparative analysis highlights that efficient thermal management via the cooling system effectively mitigates the discharge-induced temperature rise, thereby maintaining stable product distribution and preventing the deterioration of alcohol selectivity caused by overheating.

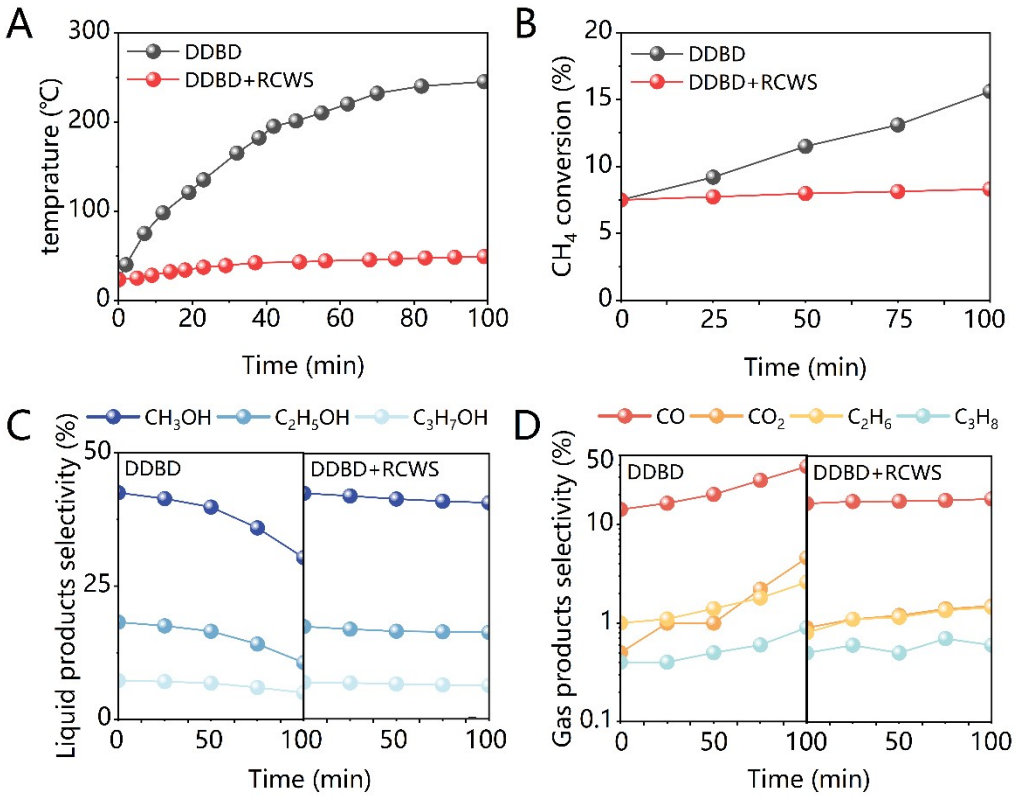

Figure S2. Long-term performance comparison between the DDBD with RCWS and the uncooled DDBD during a 100-minute continuous operation.
(A) Temperature variation in the reaction zone over time;(B) Evolution trend of CH_4 conversion; (C) Variation of liquid product selectivity;(D) Variation of gas product selectivity.

5. Calculation formula

The conversion of the reactants and the selectivity of the main products were calculated by the following equations.

The CH_4 conversion is calculated by the following equation:

$$X_{CH4} = \frac{moles\ of\ CH_4\ converted}{moles\ of\ inputed\ CH_4} \times 100\%$$

The selectivity of the products is calculated as:

$$S_{CO} = \frac{moles\ of\ CO\ produced}{moles\ of\ CH_4\ converted} \times 100\%$$

$$S_{CO_2} = \frac{moles\ of\ CO_2\ produced}{moles\ of\ CH_4\ converted} \times 100\%$$

$$S_{C_2H_6} = 2 \times \frac{moles\ of\ C_2H_6\ produced}{moles\ of\ CH_4\ converted} \times 100\%$$

$$S_{C_3H_8} = 3 \times \frac{moles\ of\ C_3H_8\ produced}{moles\ of\ CH_4\ converted} \times 100\%$$

$$S_{CH_3OH} = \frac{moles\ of\ CH_3OH\ produced}{moles\ of\ CH_4\ converted} \times 100\%$$

$$S_{C_2H_5OH} = 2 \times \frac{moles\ of\ C_2H_5OH\ produced}{moles\ of\ CH_4\ converted} \times 100\%$$

$$S_{C_3H_7OH} = 3 \times \frac{moles\ of\ C_3H_7OH\ produced}{moles\ of\ CH_4\ converted} \times 100\%$$

The carbon mass balance was calculated using the following equation:

$$B_{carbon} = \frac{\sum n_i \times M_{products}}{M_{CH4,converted}} \times 100\%$$

The energy yield was calculated according to the following formula:

$$EY(mmol/kWh) = \frac{M_{light\ alcohols}(mmol/h)}{P(kW)}$$

The selectivity for liquid products was calculated on a carbon basis, and the molar concentrations in the aqueous phase were determined using the cumulative molar amount of each species divided by the total volume of the collected solution. The molar concentrations of light alcohols are:

$$C_{total} = \Sigma \frac{(\frac{F_{CH4} \times X_{CH4}}{V_m} \times \frac{S_i}{N_i}) \times t}{V_{sol}}$$

The definitions of the physical quantities are as follows:

Symbol	Physical Meaning	Symbol	Physical Meaning
F_{CH4}	Inlet flow rate of CH_4	X_{CH4}	CH_4 conversion
V_m	Molar volume of gas	S_i	Selectivity toward product i
N_i	Number of carbon atoms in product i	V_{sol}	Total volume of the collected solution
t	Reaction duration / Collection time	C_{total}	Molar concentration of total alcohols

6. Products analysis

For the plasma-enhanced mathane steam reforming, the major liquid-phase products were identified as methanol, ethanol, and propanol, alongside minor concentrations of formic acid and formaldehyde. Meanwhile, the gas-phase effluent was found to comprise CO, CO_2, and light hydrocarbons, specifically C_2H_6, C_3H_8.

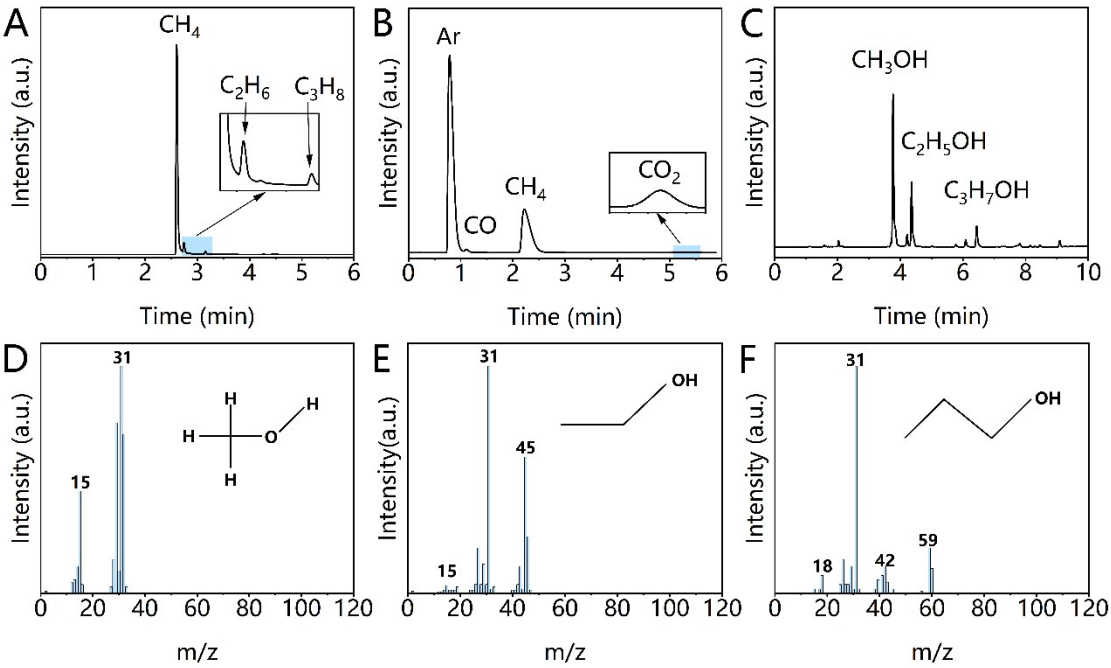

Figure S3. Qualitative analysis of products.
GC profile indicating the presence of (A) C_2H_6, C_3H_8, (B) CO, CO_2, (C)CH_3OH, C_2H_5OH, C_3H_7OH, and MS spectra of (D) CH_3OH, (E) C_2H_5OH, (F) C_3H_7OH.

7. Investigation of reaction conditions

Compared with previous reports, this work achieves a three-order-of-magnitude increase in methane conversion while maintaining product selectivity, demonstrating exceptional competitiveness.

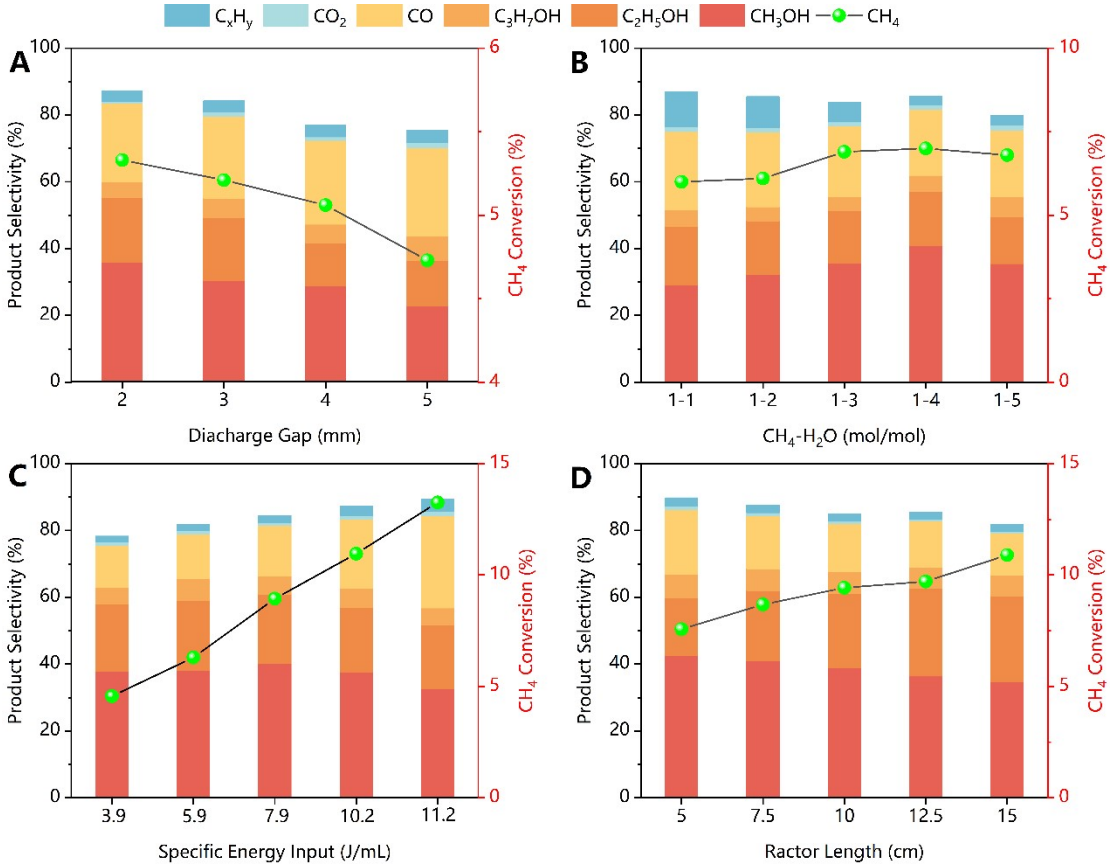

Figure S4. Investigation of reaction conditions

(A) Discharge Gap, (B) CH_4-H_2O Ratio, (C) Specific Energy Input, (D) Reactor Length.

8. Carbon balance analysis

To investigate the origin of the carbon imbalance, photographs of the metal electrode and the inner wall of the quartz reactor were taken before and after the reaction. As shown in Figure S5, a trace amount of yellowish-brown solid deposit was observed on the dielectric surfaces and electrode after extended operation, which is likely attributed to minor carbonaceous species or polymer formation. These visual evidences explain the slight deviation from a 100% carbon mass balance, confirming that while the majority of methane is converted into detectable gas and liquid products, a small fraction is deposited on the reactor internal surfaces.

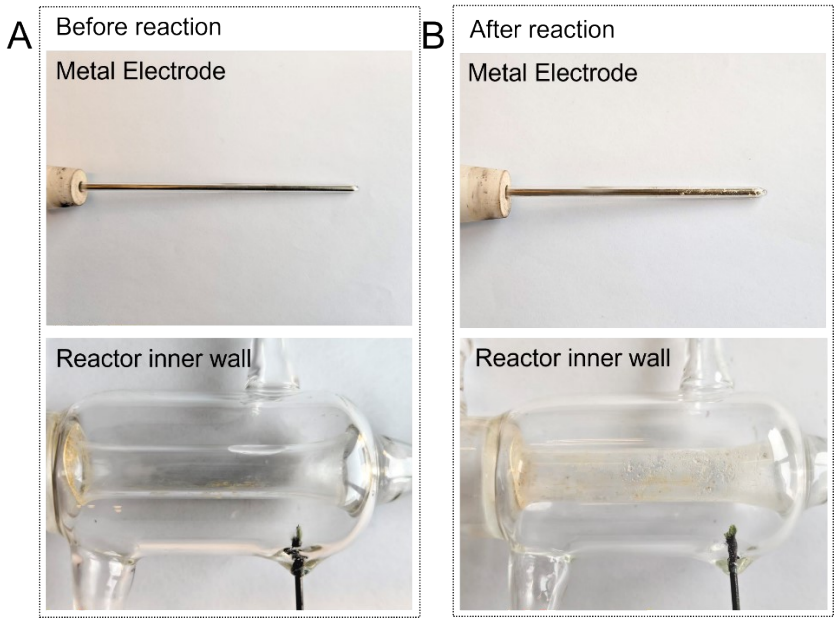

Scheme S3. Digital photographs of the (A) metal electrode and (B) quartz reactor inner wall before and after the stability test.

9. Performance comparison

The efficacy of the current DDBD reactor was evaluated by benchmarking its methane conversion and light alcohol selectivity against various state-of-the-art plasma-only and plasma-catalysis systems reported in the literature.

Table S1. Comparison of methane conversion and light alcohol selectivity between the current DDBD system and reported plasma-only or plasma-catalysis synergistic systems.

Catalyst	Reactants	CH_4 conversion	Light alcohol Selectivity	Ref
CuZrAl	CH_4, air	11	18	[1]
glass beads	CH_4, O_2	6.8	25	[2]
Mn_2O_3/glass beads	CH_4, O_2, Ar	30.5	40.2	[3]
Cu–Ni/CeO_2	CH_4, N_2O	23	36	[4]
Ga/CZA	CH_4, O_2, He	54.5	0.22	[5]
Fe_2O_3-CuO/γ-Al_2O_3	CH_4, air	25	11.33	[6]
Fe_2O_3/CP	CH_4, air	29.48	8	[7]
CuO/γ-Al_2O_3	CH_4, O_2	7.8	27	[8]
MOF-177	CH_4, O_2	23.5	17.65	[9]
Metal-containing zeolites (Fe, Pd, Mo)	CH_4, O_2	5.71	21.5	[10]
Cu/PCN	CH_4, O_2	27.6	32.9	[11]
——	CH_4, O_2	7	19	[12]
——	CH_4, O_2	4.2	38	[13]
——	CH_4, O_2	6.8	18	[14]
——	CH_4, O_2	6.5	17	[15]
——	CH_4, O_2	6.4	19	[16]
——	CH_4, O_2	9.8	20.1	[17]
——	CH_4, H_2O	2	28	[18]
——	CH_4, CO_2	18.3	11.9	[19]
——	CH_4, H_2O	2.8	58	[20]
——	CH_4, O_2	3.8	32	[21]
——	CH_4, H_2O, Ar	2.2	28	[22]
——	CH_4, CO_2	0.2	2	[23]
——	CH_4, O_2	0.26	15	[23]
——	CH_4, CO_2	18.4	11.68	[9]

10. Lissajous figures

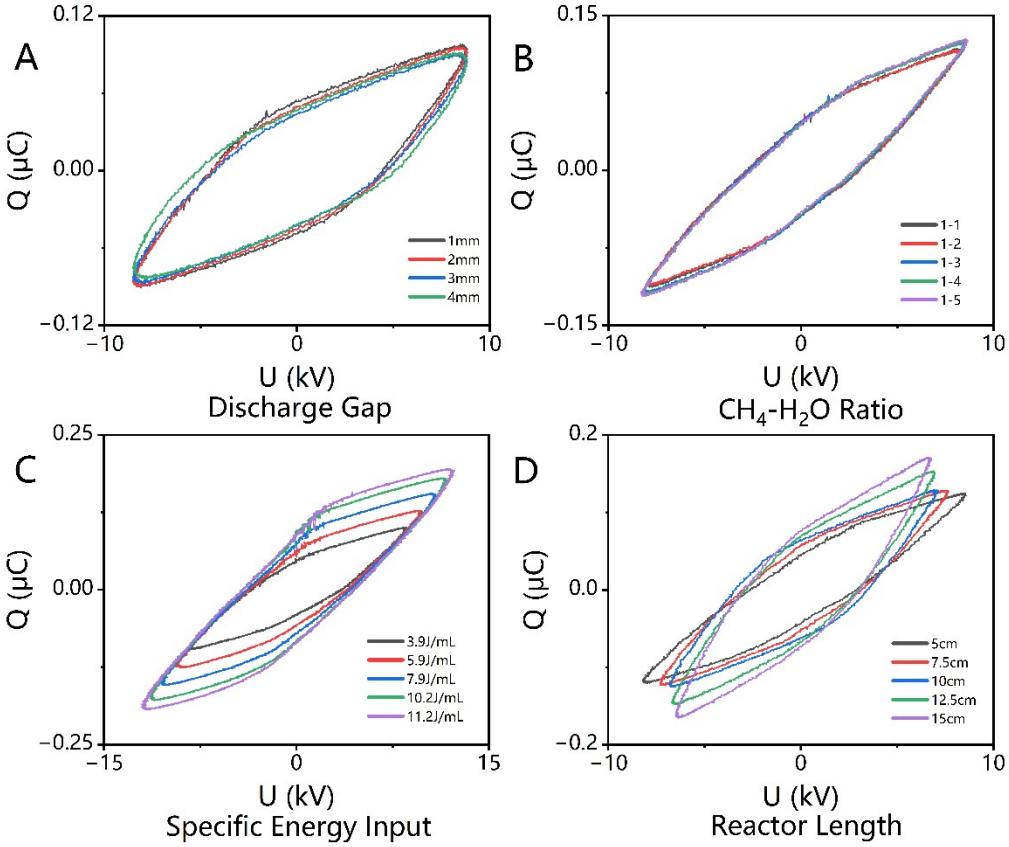

Figure S5. Lissajous figure of reaction conditions

(A) Discharge Gap, (B) CH_4-H_2O Ratio, (C) Specific Energy Input, (D) Reactor Length.

11. Current waveform diagrams

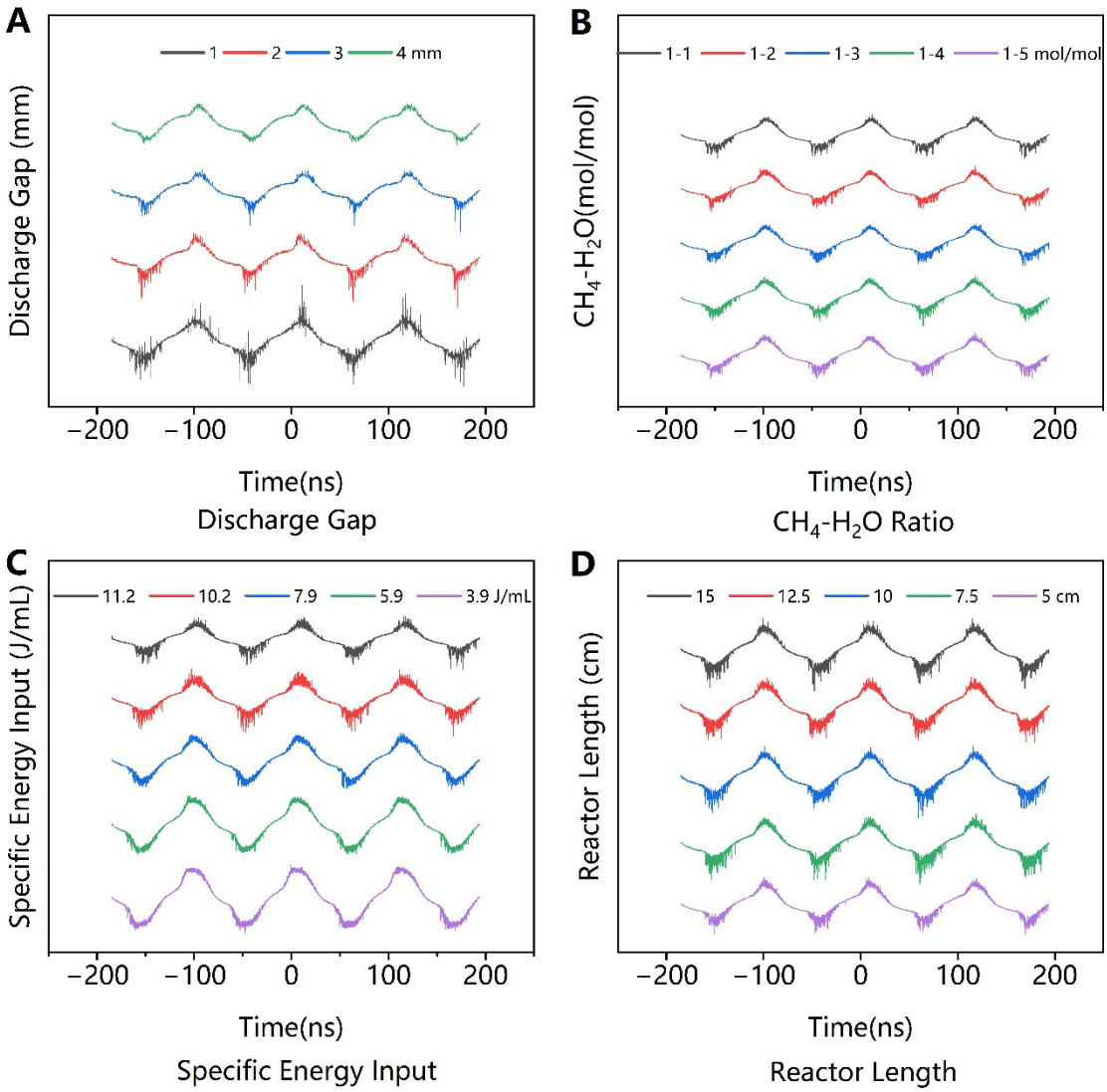

Figure S6. Current waveform diagram of reaction conditions

(A) Discharge Gap, (B) CH_4-H_2O Ratio, (C) Specific Energy Input, (D) Reactor Length.

12. *In-situ* optical emission spectra

A SP 2758 spectrometer (Princeton Instruments) was used to analyze the optical emission spectra of the $CH_4/H_2O/Ar$ plasma with wavelength from 200 to 1100 nm, aiming to diagnose active species in the $CH_4/H_2O/Ar$ plasma. A 300 $g \cdot mm^{-1}$ grating was used and the slit width of the spectrometer was fixed at 20 μm with an exposure time of 5 min.

During the optical emission spectroscopy (OES) measurements, the presence of the circulating water layer in the DDBD reactor impeded the detection of ·OH radicals. To overcome this limitation, the reactor was modified by embedding an optical window (inner diameter: 10 mm; height: 8 mm) that established direct contact with the dielectric layer. This configuration eliminated the interference from the water jacket, thereby enabling the precise measurement of ·OH species.

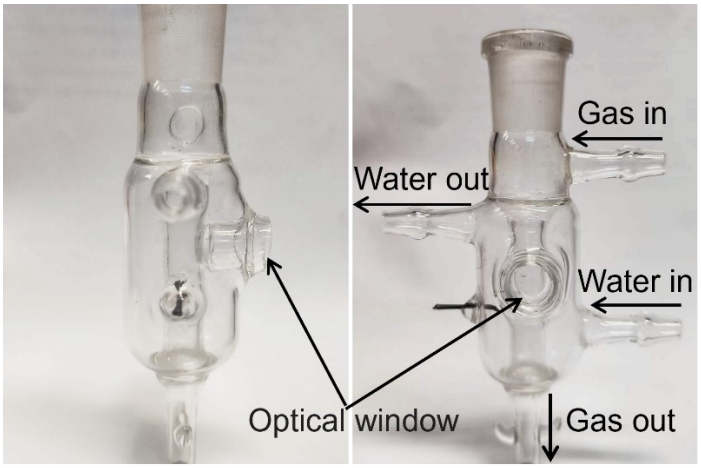

Scheme S4. External view of the DDBD reactor featuring an optical window.

13. *In-situ* Fourier transform infrared spectroscopy

In the *in-situ* FTIR device, the plasma was generated between the high voltage electrode and the ground electrode. Reaction was carried out in the FTIR reaction cell as shown in Scheme S4. Prior to the measurement, methane and argon gas were injected to purge the air for 30min. At the same time, the gasification temperature of the steam generator and the heat strip temperature were raised to 115 ℃. The instrument parameters are set to 8 cm^{-1} optical resolution and 8 scans, and the scan range was 4000-900 cm^{-1}. The background was collected after the raw gas (CH_4/Ar/H_2O) was injected for 10 min. At the same time, the plasma was turned on, and the FTIR spectrometer (Nicolet iS10, Thermo Scientific) was employed to automatically collect IR signals of the species in the gas phase using an OMNIC software. The discharge power was maintained at 30W, and the discharge was stopped after the reaction for 30 min.

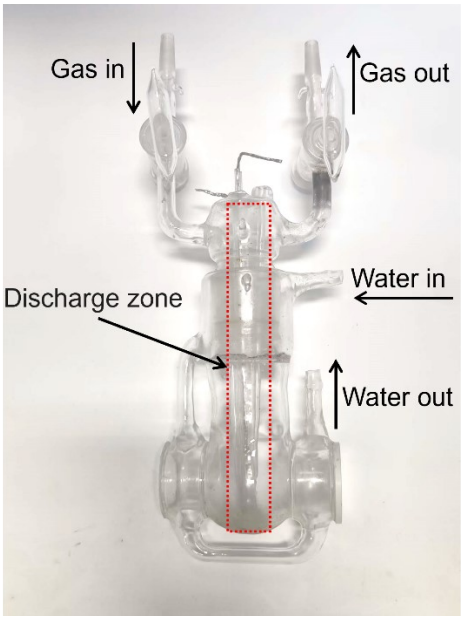

Scheme S5. Schematic diagram of the *in-situ* FTIR reaction cell.

14. *In-situ* molecular beam mass spectrometry

A novel *in-situ* molecular beam mass spectrometry (MBMS) system was developed comprising a custom-designed quartz dielectric barrier discharge reactor coupled with a vacuum ultraviolet photoionization time-of-flight mass spectrometer (VUV-PI-TOFMS). This configuration utilizes a supersonic expansion technique to facilitate rapid transport of excited species and short-lived radicals from the atmospheric pressure reaction zone to the high-vacuum detection chamber with minimal collisions, thereby effectively suppressing secondary reactions during transmission and preserving their nascent chemical states.

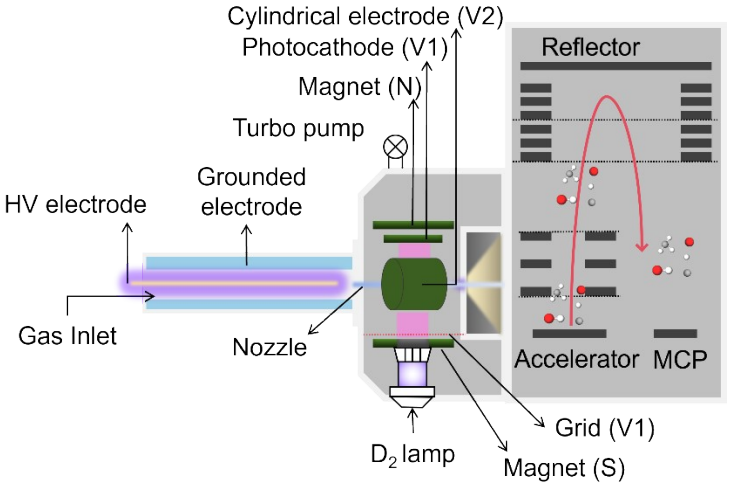

Scheme S6. Schematic diagram of the *in-situ* MBMS system.

15. Nuclear magnetic resonance

Nuclear magnetic resonance (NMR) characterization was performed using a 600 MHz fully digital superconducting NMR spectrometer (equipped with TopSpin version 4.0.5 software for data acquisition and processing). The system featured a 5 mm high-sensitivity TCI cryoprobe, enabling high-resolution analysis of 1H, 14C, and 15N nuclei. Technical specifications included a 1H non-spinning resolution of < 0.7Hz and a line-shape of < 7/14Hz. The instrument demonstrated superior sensitivity, with a 1H sensitivity of >6800. Variable temperature experiments were supported across a range of -150℃ to 150℃. Comprehensive structural elucidation was achieved through 1D spectroscopy and a suite of 2D correlation experiments, including 1H-H (COSY, NOESY, ROESY, TOCSY) and 1H-X (HSQC, HMBC) techniques, utilizing a 24-slot autosampler for automated high-throughput analysis.

16. Electron paramagnetic resonance

Electron paramagnetic resonance (EPR) measurements were conducted using a Bruker E500 spectrometer (Bruker Scientific Technology Co., Ltd., Beijing, China) operating in the X-band (9.2-9.9 GHz). The system is characterized by a magnetic field range of 0-1.45T with a high sweep resolution of 128,000 points and a detection sensitivity of 1×10^9 spins/G. Comprehensive variable-temperature analysis was facilitated by liquid nitrogen and liquid helium cryostat attachments, supporting temperature ranges of 100K to 600K and 4.2K to 300K, respectively. The instrument is further equipped for in-situ illumination experiments, enabling the real-time detection and characterization of free radicals and triplet state molecules, including their concentration, lifetime, and spatial distribution. This setup was utilized to investigate the ground-state spectra, spin states, g-values, and relaxation processes of paramagnetic ions, as well as to probe semiconductor band structures and conduction mechanisms.

17. Gas Chromatography-Mass Spectrometry

Chemical analysis and characterization were conducted using an Agilent 5975C Gas Chromatography-Mass Spectrometry (GC-MS) system (Agilent Technologies, Santa Clara, CA, USA). The instrument features a patented gold-plated quartz hyperbolic quadrupole, which enhances both performance and reliability while supporting a mass scanning range up to 1050 u. The system is equipped with a monolithic inert ion source capable of operating at temperatures up to 350°C, ensuring consistent results for diverse analytes. A Triple-Axis HED-EM detector provides superior sensitivity and a reduced signal-to-noise ratio, demonstrated by a specification of 200:1 for 1 pg of octafluoronaphthalene (OFN). High-performance electronics allow for rapid data acquisition with scan speeds reaching 12,500 u/s. Furthermore, the spectrometer supports simultaneous SIM/Scan modes and features automated SIM method development, facilitating efficient qualitative and quantitative structural analysis.

18. ·OH quenching experiment

Experimental Procedure for ·OH Quenching

1. Preparation of Scavenger Solutions:

Three aqueous solutions of isopropanol (IPA) were prepared with mass fractions of 0.5%, 1%, and 2%. The solutions were synthesized by accurately weighing the required amount of high-purity IPA and mixing it with deionized water to ensure precise concentrations.

2. Feeding and Preheating:

The IPA-water mixture was introduced into the reaction system using a high-precision syringe pump. The liquid feed was directed into a preheater/evaporator (typically maintained at a temperature above 120℃) to ensure complete vaporization. Simultaneously, the reactant gas was regulated by a mass flow controller (MFC) and mixed with the superheated steam containing the IPA scavenger.

3. Reaction Execution:

The gas-phase mixture was fed into the fixed-bed reactor. The reaction was conducted at the specified temperature and pressure parameters optimized for methane-to-methanol conversion. To maintain a steady state, the system was allowed to stabilize for at least 30-60 minutes at each IPA concentration before sampling.

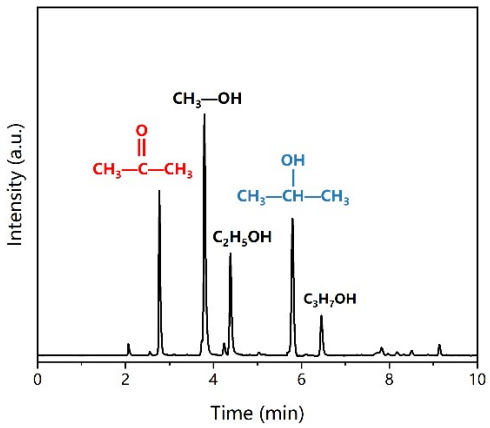

Figure S7. ·OH quenching experiment.

19. Density functional theory calculations

All density functional theory (DFT) calculations were carried out using the CP2K 2022 package[24]. The Gaussian and plane waves (GPW) method was employed to model the electronic structure[25]. The exchange-correlation interactions were described using the generalized gradient approximation (GGA) parameterized by Perdew, Burke, and Ernzerhof (PBE), combined with Grimme's DFT-D3 dispersion correction with Becke–Johnson damping (D3-BJ) to account for weak van der Waals interactions[26, 27].

The core electrons were modeled using Goedecker–Teter–Hutter (GTH) norm-conserving pseudopotentials, while the valence electrons were expanded using molecularly optimized triple-ζ valence polarized basis sets (TZVP-MOLOPT-GTH) for C, H, and O atoms[28]. The cutoff energy for the auxiliary plane-wave basis set was set to 600 Ry. The calculations were performed using the unrestricted Kohn-Sham (UKS) formalism to correctly describe the open-shell radical species $\cdot CH_3$, $\cdot C_2H_5$, $\cdot C_3H_7$, and $\cdot OH$.

Geometry optimizations were performed using the BFGS optimizer[29]. A cubic simulation cell with a side length of 15 Å was used, and periodic boundary conditions were applied in all three directions with a Poisson solver. Frequency calculations were performed to confirm that the optimized structures correspond to local minima (no imaginary frequencies) and to obtain zero-point energy (ZPE) and thermal corrections to the Gibbs free energy at 298 K.

20. Glossary of terms and abbreviations

Table S2. Summary of technical terms, abbreviations

Abbreviation	Full Technical Term
SDBD	Single Dielectric Barrier Discharge
DDBD	Double Dielectric Barrier Discharge
RCWS	Recirculating Cooling Water System
DOM	Direct Oxidation of Methane
NTP	Non-Thermal Plasma
FID	Flame Ionization Detector
TCD	Thermal Conductivity Detector
GC-MS	Gas Chromatography-Mass Spectrometry
OES	Optical Emission Spectroscopy
FITR	Fourier Transform Infrared Spectroscopy
MBMS	Molecular Beam Mass Spectrometry
EPR	Electron Paramagnetic Resonance
MS	Mass Spectrometry
IPA	Isopropyl Alcohol
NMR	Nuclear Magnetic Resonance
DFT	Density Functional Theory
SEI	Specific Energy Input
EY	Energy Yield

References

1. P. Chawdhury, D. Kumar and C. Subrahmanyam, *Chemical Engineering Journal*, 2019, **372**, 638-647.
2. P. Chawdhury, D. Ray and C. Subrahmanyam, *Fuel Processing Technology*, 2018, **179**, 32-41.
3. H. Lee and D. H. Kim, *Scientific Reports*, 2018, **8**, 9956.
4. S. Mahammadunnisa, K. Krushnamurty and C. Subrahmanyam, *Catalysis Today*, 2015, **256**, 102-107.
5. A. Indarto, *Ionics*, 2014, **20**, 445-449.
6. L. Chen, X. Zhang, L. Huang and L. Lei, *Chemical Engineering & Technology*, 2010, **33**, 2073-2081.
7. L. Chen, X.-W. Zhang, L. Huang and L.-C. Lei, *Chemical Engineering and Processing: Process Intensification*, 2009, **48**, 1333-1340.
8. P. Chawdhury, D. Ray, T. Vinodkumar and C. Subrahmanyam, *Catalysis Today*, 2019, **337**, 117-125.
9. F. Gorky, A. Nambo and M. L. Carreon, *Journal of CO2 Utilization*, 2021, **51**, 101642.
10. D. Lašič Jurković, H. Puliyalil, A. Pohar and B. Likozar, *International Journal of Energy Research*, 2019, **43**, 8085-8099.
11. C. Qi, Y. Xing, H. Yu, Y. Bi, P. Zhou, H. Wu, R. Guo, H. Zhang, M. Wu and W. Wu, *Industrial & Engineering Chemistry Research*, 2022, **61**, 16635-16642.
12. P. Chawdhury, K. V. S. S. Bhargavi, M. Selvaraj and C. Subrahmanyam, *Catalysis Science & Technology*, 2020, **10**, 5566-5578.
13. Y. Yi, S. Li, Z. Cui, Y. Hao, Y. Zhang, L. Wang, P. Liu, X. Tu, X. Xu, H. Guo and A. Bogaerts, *Applied Catalysis B: Environmental*, 2021, **296**, 120384.
14. P. Chawdhury, K. V. S. S. Bhargavi and C. Subrahmanyam, *Catalysis Communications*, 2020, **147**, 106139.
15. P. Chawdhury, Y. Wang, D. Ray, S. Mathieu, N. Wang, J. Harding, F. Bin, X. Tu and C. Subrahmanyam, *Applied Catalysis B: Environmental*, 2021, **284**, 119735.
16. P. Chawdhury, K. V. S. S. Bhargavi and C. Subrahmanyam, *Sustainable Energy & Fuels*, 2021, **5**, 3351-3362.
17. D. W. Larkin, L. L. Lobban and R. G. Mallinson, *Catalysis Today*, 2001, **71**, 199-210.
18. Y. Hao, S. Li, W. Fang, X. Wang, Z. Cui, K. M. Bal, N. Gerrits, H. Guo, E. C. Neyts, A. Bogaerts and Y. Yi, *AIChE Journal*, 2024, **71**.
19. L. Wang, Y. Yi, C. Wu, H. Guo and X. Tu, *Angewandte Chemie International Edition*, 2017, **56**, 13679-13683.
20. Y. Tang, Y. Cui, G. Ren, K. Ma, X. Ma, C. Dai and C. Song, *Fuel Processing Technology*, 2023, **244**, 107722.
21. H. Lv, X. Liu, Y. Hao and Y. Yi, *Plasma Chemistry and Plasma Processing*, 2023, **43**, 1963-1978.
22. W. Fang, X. Wang, S. Li, Y. Hao, Y. Yang, W. Zhao, R. Liu, D. Li, C. Li, X. Gao, L. Wang, H. Guo and Y. Yi, *Green Chemistry*, 2024, **26**, 5150-5154.
23. C. De Bie, J. van Dijk and A. Bogaerts, *The Journal of Physical Chemistry C*, 2015, **119**, 22331-22350.
24. J. Hutter, M. Iannuzzi, F. Schiffmann and J. VandeVondele, *WIREs Computational Molecular Science*, 2014, **4**, 15-25.
25. J. VandeVondele and J. Hutter, *The Journal of Chemical Physics*, 2007, **127**, 114105.

26. J. P. Perdew, K. Burke and M. Ernzerhof, *Physical Review Letters*, 1996, **77**, 3865-3868.
27. S. Grimme, J. Antony, S. Ehrlich and H. Krieg, *The Journal of Chemical Physics*, 2010, **132**, 154104.
28. S. Goedecker, M. Teter and J. Hutter, *Physical Review B*, 1996, **54**, 1703-1710.
29. J. D. Head and M. C. Zerner, *Chemical Physics Letters*, 1985, **122**, 264-270.